



12-1-2020

Fundamental electronic structure and multiatomic bonding in 13 biocompatible high-entropy alloys

Wai Yim Ching

Saro San

Jamieson Brechtel

Ridwan Sakidja

Missouri State University

Miqin Zhang

See next page for additional authors

Follow this and additional works at: <https://bearworks.missouristate.edu/articles-cnas>

Recommended Citation

Ching, Wai-Yim, Saro San, Jamieson Brechtel, Ridwan Sakidja, Miqin Zhang, and Peter K. Liaw.

"Fundamental electronic structure and multiatomic bonding in 13 biocompatible high-entropy alloys." npj Computational Materials 6, no. 1 (2020): 1-10.

This article or document was made available through BearWorks, the institutional repository of Missouri State University. The work contained in it may be protected by copyright and require permission of the copyright holder for reuse or redistribution.

For more information, please contact BearWorks@library.missouristate.edu.

Authors

Wai Yim Ching, Saro San, Jamieson BrechtI, Ridwan Sakidja, Miqin Zhang, and Peter K. Liaw

ARTICLE OPEN



Fundamental electronic structure and multiatomic bonding in 13 biocompatible high-entropy alloys

Wai-Yim Ching^{1✉}, Saro San¹, Jamieson Brechtel², Ridwan Sakidja³, Miqin Zhang⁴ and Peter K. Liaw⁵

High-entropy alloys (HEAs) have attracted great attention due to their many unique properties and potential applications. The nature of interatomic interactions in this unique class of complex multicomponent alloys is not fully developed or understood. We report a theoretical modeling technique to enable in-depth analysis of their electronic structures and interatomic bonding, and predict HEA properties based on the use of the quantum mechanical metrics, the total bond order density (TBOD) and the partial bond order density (PBOD). Application to 13 biocompatible multicomponent HEAs yields many new and insightful results, including the inadequacy of using the valence electron count, quantification of large lattice distortion, validation of mechanical properties with experiment data, modeling porosity to reduce Young's modulus. This work outlines a road map for the rational design of HEAs for biomedical applications.

npj Computational Materials (2020)6:45; <https://doi.org/10.1038/s41524-020-0321-x>

INTRODUCTION

High-entropy alloys (HEAs) are complex metallic alloys^{1–4} comprised of four, five, or more principal components of different concentrations. Such a structure leads to a high mixing entropy that favors the formation of single phase disordered solid solutions at higher temperatures^{5,6}, although the enthalpy also plays a critical role in determining its composition and phase with no long-range-order (LRO)^{1,7}. A significant amount of disorder exist in HEAs when they undergo elemental segregation, precipitation, and chemical ordering, but uncertainty remains regarding the existence and the nature of short-range-orders (SRO)⁸. The fundamental theory for the formation of HEAs is not fully established despite many theories and modeling efforts since their inception^{9–12}. Due to the complexity of their compositions and the difficulties for accurate measurements for comparison, most of these efforts are based on different perspectives and quite scattered. They generally used the random solid-solution-model (RSSM) to evaluate their properties although the methods employed could be very different^{13–15}. Current theoretical methods for HEAs are spread out and include but not limited to the use of CALPHAD^{1,12,16}, quasi-random-structure (SQS)^{17–19} usually in the framework of density functional theory (DFT) on small-size supercells²⁰, coherent potential approximations (EMTO-CPA) or effective medium theory^{21,22}. Despite a plethora of approaches and methods used, few of them can provide a comprehensive view on their formation and the prediction of their properties due to several obstacles. Firstly, due to relatively large chemical disorder in HEAs, the application of RSSM requires using large supercells. Secondly, the computational demand for accurate large-scale DFT calculations could be prohibitive. Finally, the lack of a non-empirical metric to interpret the results that involve subtle interactions between different metal atoms. By introducing the concept of total bond order density (TBOD) and partial bond order density (PBOD) based on the quantum-mechanical (QM) metrics (see the “Methods” section), we avoid

the use of pure geometric parameters in describing the structures, compositions, and properties of HEAs. The new perspective is based on the understanding the nature of metallic bonding, crucially related to the theory of formation of HEAs. Although metallic bonding has been extensively discussed in the field of metallic glasses (MGs)^{23,24}, it has not been thoroughly investigated for HEAs. Metallic bonding is multi-atomic in nature, different from the covalent or ionic bonding where the bond length (BL) is explicitly defined as the distance between the two atoms forming the bond. In MGs, and to a lesser extent in HEAs, the BL can be ambiguous, since all atoms within a certain distance of separation can contribute to metallic bonding. For a fixed distance of separation for a pair of atoms in the model, there could be many possible values of bond order (BO), a measure of the bond strength; and for a specific value of BO, there could be many possible pairs of atoms with the same distance of separation. A theory that is predominately depending on the geometric parameter of BL, or atomic size for interpretation could be oversimplified and problematic. On the other hand, the concept of the TBOD is still applicable as long as the BO values of all the contributing atoms are counted. This point has already been strongly argued for in reference²⁵ for MG. What differentiate HEAs from MGs is that HEAs have a basic crystal lattice (FCC, BCC, or HCP) as its structural backbone. However, based on the RSSM description, HEAs are not strictly crystalline. They possess no LRO and negligible or small SRO with different nearest neighbor (NN) and second nearest neighbor (SNN) pairs. This is the same predicament facing the vague description of the so-called lattice distortion (LD) that will be discussed later. The use of TBOD and its partial components, the PBOD, to explore the theory of formation in HEAs is clearly a novel approach.

As the populations of developed countries continue to age, there is an increasing demand for biocompatible implant materials. Traditionally, stainless steels and titanium alloys have been typically implemented as joint surrogate metals^{26,27}. More recently HEAs^{5,7} have been proposed as viable candidates due to

¹Department of Physics and Astronomy, University of Missouri Kansas City, Kansas City, MO 64110, USA. ²The Bredesen Center for Interdisciplinary Research and Graduate Education, The University of Tennessee, Knoxville, TN 37996-3394, USA. ³Department of Physics, Astronomy and Materials Science, Missouri State University, Springfield, MO 65897, USA. ⁴Department of Materials Science and Engineering, The University of Washington, Seattle, WA 98195, USA. ⁵Department of Materials Science and Engineering, The University of Tennessee, Knoxville, TN 37996-2100, USA. ✉email: chingw@umkc.edu

their favorable properties, such as high strength and ductility, resistance to corrosion, wear, and fatigue. Importantly, HEAs may consist of refractory elements that are mostly non-toxic and hypoallergenic. They favor the structure of a single solid-solution phase in BCC lattice and have been proposed as a new class of metallic biomaterials²⁸. With Mo present, it exhibited excellent biocompatibility compared to the pure Ti²⁸. However, the Young's modulus of this alloy system is roughly 10 times greater than human bones²⁹. Other challenges including the structural complexity involved at the interfaces with tissues and bones, and other soft matters in an aqueous environment involving body fluids.

In this article, we present the results on the electronic structure, interatomic bonding, and the application of TBOD and PBOD in addressing the challenges for fundamental understanding on the theory of formation of HEAs and its potential applications. We would like to point out the special merits of using TBOD and PBOD as key metrics for assessing the fundamental properties of multicomponent alloys (see "Methods" section for detail). They can be directly compared with each other irrespective of their atomic species, composition, or size. Moreover, they can be applied to other materials systems as long as all interatomic bonding between every pair of atoms are included and normalized by the volume of the cell. This characteristic is very different from other techniques based on ground state energies used in the enthalpy evaluation^{19,30,31}. The total energies for different HEAs can be very different because of the difference in the reference energies, although the formation energy for each HEA can explicitly be calculated, which can be quite onerous and time consuming for multi-component HEAs with different compositions. Also, the PBOD resolved from the TBOD have different pairwise components is particularly useful in revealing the details of the interatomic interactions, since TBOD and PBOD are derived from quantum mechanical calculations, not from geometric parameters. Such information cannot be obtained easily based on the calculation of total energies.

In the present work, the electronic structures, interatomic bonding, and mechanical properties of the 13 bioinspired HEAs (Table 1) are investigated through advanced modeling using large supercells yielding many new and insightful results critical to the development and application of biocompatible HEAs.

RESULTS

Electronic structure and interatomic bonding

We start the "Results" section with the central part of this paper, the electronic structure, and interatomic bonding. The results for the 13 HEAs constitute a substantial amount of data. Model M3 (TiNbTaZrMo) is chosen as a representative one (Fig. 1) for focused presentation of the results. They are sketch of the supercell structure of 250 atoms (Fig. 1a), total and partial density of states (DOS) (Fig. 1b), partial charge (PC) distribution (Fig. 1c), and results related to interatomic bonding (Fig. 1d, e). Results for other HEAs are presented in (Figs. S1, S2, and S4). The data on TDOS values at the Fermi level E_F ($N(E_F)$) and the minimum values at the locations of the deep valley in the conduction band (CB) above E_F of the 13 HEAs are listed in Supplementary Table 1. The similarity in the DOS features amongst the 13 HEAs for energies ranging from -5 to $+5$ eV is because they are all derived from the $3d/4d/5d$ orbitals of the transition metals in the HEAs.

An important electronic structural property is the effective charge Q^* associated with the so-called PC $\Delta Q = (Q^0 - Q^*)$ where Q^0 is the charge of the neutral atom also called the valence electron count (VEC) (see "Methods" section). Figure 1c displays the PC distribution of the 250 atoms in M3. Similar plots for other HEAs are shown in Supplementary Fig. 2. Table 2 lists the averaged PC and Q^* for each atomic component in the 13 HEAs. We then average them over the HEAs containing that element (bottom of Table 2 and above the row for VEC). As can be seen, Ti, V, Zr, and Hf have a VEC of 4, Nb and Ta have a VEC of 5, and Mo has a VEC of 6. The calculated Q^* values range from 4.10 (M3) to 4.37 (M9) for Ti; 4.09 (M1) to 4.25 (M4) for V; 3.67 (M3) to 3.87 (M9) for Zr, and 3.51 (M10, M13) to 3.72 (M9) for Hf, respectively. These Q^* values depend on the compositions of the HEAs. The increases in Q^* (Ti, Ta, V, and Mo) or decreases in Q^* (Nb, Zr, and Hf) beyond their VEC depend on the atomic compositions and specific HEAs involved. The averaged Q^* of each type of atoms for all 13 HEAs show significant deviations from VEC (Supplementary Fig. 3). This trend strongly suggests that conventional theories using VEC as the key parameter in their formulation may be inadequate and is the main reason for the failure of using the rule of mixture (ROM) in the explanation of simulation results in other studies^{32,33}. The trend is also particularly true in some more complicated HEAs with specific local structures, such as those involving defects or other microstructures. Since the entire HEA system should be electrically neutral with a zero net charge, a slight deviation in the atomic

Table 1. Fully relaxed structures for the 13 biocompatible models.

Models		C	<i>a</i> (Å)	<i>b</i> (Å)	<i>c</i> (Å)	α	β	γ	Vol (Å ³)	NN (Å)	SNN (Å)
M1	TiNbTaV	4	16.104	16.066	16.084	90.049	89.522	90.288	4161.047	2.786	3.217
M2	TiNbTaZr	4	16.793	16.755	16.845	90.002	89.902	90.400	4739.407	2.909	3.360
M3	TiNbTaZrMo	5	16.600	16.509	16.560	89.566	90.138	90.134	4537.862	2.868	3.311
M4	HfNbTaV	4	16.525	16.458	16.480	90.121	89.870	90.523	4481.912	2.856	3.298
M5	NbTaTiVZr	5	16.546	16.432	16.459	89.881	89.864	90.136	4474.812	2.854	3.296
M6	TiZrHfNbTa	5	16.874	17.115	16.987	89.696	90.083	90.161	4905.735	2.943	3.398
M7	TiHfNbTa	4	16.734	16.749	16.767	89.974	89.902	90.457	4699.020	2.901	3.350
M8	TiZrHfTa	4	17.197	17.168	17.027	90.103	89.471	89.909	5026.873	2.967	3.426
M9	TiZrHfNb	4	17.153	17.124	17.066	90.196	89.515	90.087	5012.223	2.964	3.423
M10	TiZrMoHfTa	5	16.806	16.757	16.836	89.752	90.128	90.199	4741.094	2.910	3.360
M11	ZrNbMoHfTa	5	16.775	16.808	16.934	89.862	90.099	90.111	4774.622	2.917	3.368
M12	TiZrNbMoHf	5	16.731	16.728	16.928	89.820	90.175	90.216	4737.708	2.909	3.359
M13	TiNbMoHfTa	5	16.479	16.519	16.550	89.662	90.233	90.166	4504.892	2.861	3.303

The NN and SNN stand for the average distances of nearest neighbors (NN), and second nearest neighbors (SNN). The elements involved are Ti, V, Zr, Nb, Mo, Hf, and Ta and 'C' stands for components. M1 (M8) has the smallest (largest) volume.

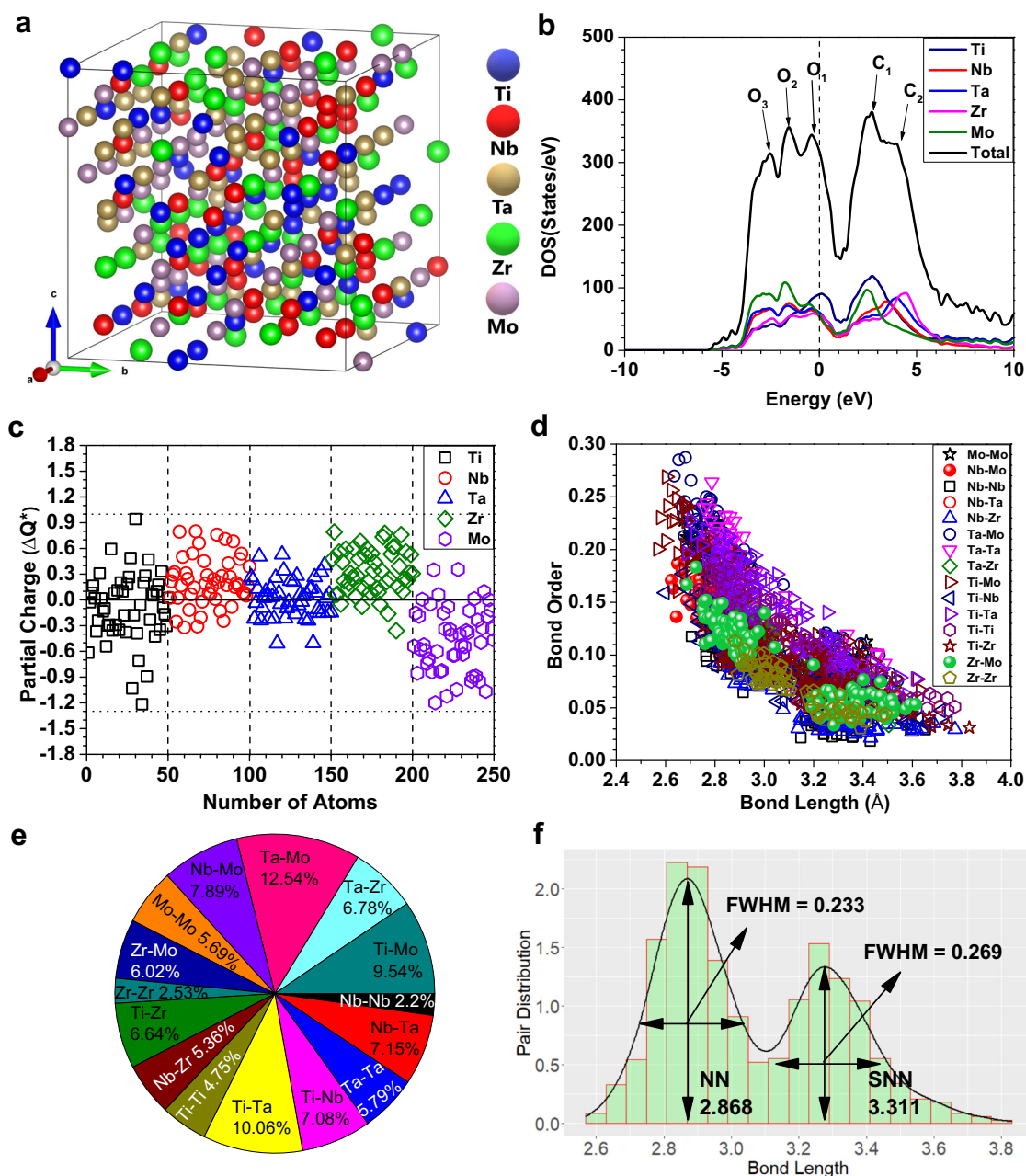


Fig. 1 Electronic structure and bonding in M3. **a** Ball and stick sketch of the supercell. **b** TDOS and atom-resolved PDOS. The zero energy corresponds to the Fermi level E_F . The magnitude of DOS at E_F , $N(E_F)$ correlates with electric conductivity of the alloy. Peaks are marked as O₁, O₂, and O₃ at -0.39 , -1.56 , and -2.53 eV below E_F , and C₁ and C₂ at 2.70 and 3.98 eV above E_F . **c** Partial charge distribution of 250 atoms in five metals. They can be either positive or negative. **d** BO vs. "BL" distribution between all atomic pairs among 15 possible types. **e** Percentage contribution of PBOD to TBOD for each type. Ta-Mo has the largest contributions (12.54%) and Nb-Nb the smallest (2.2%). **f** FWHM for the two Gaussians fitted to the histogram distribution of the average NN and SNN the interatomic distances. The two FWHMs are 0.233 and 0.269 Å with an average value of 0.250 Å. This provides the quantitative measure of the lattice distortion in HEAs.

composition can offer opportunities for fine-tuning their targeted properties. Atom-specific effective charge Q^* can also be used as a descriptor in the machine-learning (ML) technique but they are less important than the TBOD and PBOD.

The distribution of the BO vs. the bond length ("BL") for all interatomic pairs up to a "BL" of 4.0 Å in M3 is shown in Fig. 1d. The "BL" (with quotation) is the distance of separation between a pair of atoms with a specific BO value. These BOs are calculated with contributions from all atoms near this particular pair since metallic bonding is multiatomic, not pairwise. The TBOD is

determined by the strength of all interatomic bonds and their propensity normalized by the cell volume (see "Methods" section). The contributions from the specific PBOD that are decomposed from the TBOD is depicted in the pie chart (Fig. 1e). Similar BO vs. "BL" plots and pie charts for other HEAs are shown in Supplementary Fig. 4.

The TBOD and PBOD in the 13 biocompatible HEAs are presented in the form of histogram bars (Fig. 2a) and pie chart (Fig. 2b). This complex display requires the detailed analysis to appreciate the information that it contains. Some of the general

Table 2. List of effective charge for each element.

Models	Ti		Nb		Ta		V		Zr		Hf		Mo	
	PC	Q*	PC	Q*	PC	Q*	PC	Q*	PC	Q*	PC	Q*	PC	Q*
M1	−0.12	4.12	0.19	4.81	0.01	4.99	−0.09	4.09	−	−	−	−	−	−
M2	−0.22	4.22	0.11	4.89	−0.13	5.13	−	−	0.24	3.76	−	−	−	−
M3	−0.10	4.10	0.21	4.79	0.02	4.98	−	−	0.33	3.67	−	−	−0.46	6.46
M4	−	−	0.05	4.95	−0.20	5.20	−0.25	4.25	−	−	0.39	3.61	−	−
M5	−0.19	4.19	0.14	4.86	−0.06	5.06	−0.16	4.16	0.27	3.73	−	−	−	−
M6	−0.31	4.31	0.02	4.98	−0.23	5.23	−	−	0.17	3.83	0.35	3.65	−	−
M7	−0.28	4.28	0.08	4.92	−0.19	5.19	−	−	−	−	0.39	3.61	−	−
M8	−0.34	4.34	−	−	−0.22	5.22	−	−	0.19	3.81	0.37	3.63	−	−
M9	−0.37	4.37	−0.03	5.03	−	−	−	−	0.13	3.87	0.28	3.72	−	−
M10	−0.16	4.16	−	−	−0.08	5.08	−	−	0.31	3.69	0.49	3.51	−0.56	6.56
M11	−	−	0.10	4.90	−0.17	5.17	−	−	0.25	3.75	0.43	3.57	−0.61	6.61
M12	−0.19	4.19	0.10	4.90	−	−	−	−	0.25	3.75	0.42	3.58	−0.58	6.58
M13	−0.12	4.12	0.18	4.82	−0.05	5.05	−	−	−	−	0.49	3.51	−0.51	6.51
Ave.	−0.22	4.22	0.10	4.90	−0.12	5.12	−0.17	4.17	0.24	3.76	0.40	3.60	−0.54	6.54
VEC	4		5		5		4		4		4		6	

Comparison of effective charge (Q*) and partial charge (PC) with the valence electron count (VEC) for each atom in the 13 biocompatible HEA models.

trends are discussed in the figure caption. Still, we cannot be certain about whether there exists any trends related to their composition, atomic species, and their interatomic interactions in relation to PBOD. This critical issue will require a more penetrating analysis. An interesting issue frequently discussed in the HEA community is the possible existence of SRO and if we can quantify it. A commonsense rule is to consider that a single atom has no SRO, or the short-range-order-parameter $SROP = 0$, and a diatomic molecule has the maximum $SROP = 1$. The SROP in HEAs can be obtained from the root-mean-square (RMS) deviation of [PBOD/TBOD]. First, the ratio of PBOD/TBOD for each of the 13 models are calculated from the data listed in the table of Fig. 2a. Next the RMS value for each model are calculated and listed in Supplementary Table 1. As can be seen, they exclusively depend on the number of atomic components. The 4-component and 5-component HEAs have $SROP = 0.11$ and 0.07 , respectively. The larger the atomic components, the lower the SROP. We thus conclude that SRO in HEAs under the RSSM is very small. Since the TBOD and PBOD are obtained from QM calculations of individual BO values, therefore provide the vitally important details regarding the nature of the formation of HEAs. This is consistent with the notion of order emerging from disorder for a broader class of functionalized HEAs³⁴. It should also be pointed out that the above description is strictly based on the homogenized RSSM used in the supercell and does not apply to cases where there may involve other factors under different assumptions^{8,35}. Experimentally, the actual sample will be much larger and may involve multiphase structures, the presence of impurities or dislocations that may induce some form of SRO beyond the simple notion of number of atomic components. The present method of quantifying SRO could still be applied in such a scenario as long as the supercell itself contains far more complicated nonhomogeneous structures beyond the RSSM.

Lattice distortion

LD plays a central role in controlling the properties of HEAs³⁶. A large LD could be the harbinger of a possible phase transition or sample inhomogeneity. However, the degree of LD in HEAs is difficult to quantify beyond the geometric parameters (Table 1).

We can quantify LD from the BO vs. “BL” data (Fig. 1d and Supplementary Fig. 4) by resolving them into interatomic pairs. For M3, the scattered plot shows that Ti–Zr, Ti–Ti, and Ti–Nb pairs from NN and SNN groups start to merge (Supplementary Fig. 4c). This is a strong evidence of large LD. Similar observations for other HEAs are displayed in Supplementary Fig. 4a–h. The investigations on LD reported in the literature are mostly vague and sometimes misleading. The difficulty in providing a more precise description for LD arises from the lack of a basic reference for the undistorted lattice for HEAs due to the random distributions of the different metallic ions of varying sizes throughout the lattice. In other words, there is no such a thing as an undistorted lattice to be used as a reference. To quantify the notion of LD, the histogram distribution of “BL” of interatomic pairs in M3 is plotted (Fig. 1f). The data are fitted with two Gaussians exhibiting a bimodal distribution for the NNN and SNN pairs. The larger the two FWHM and their sum, the greater the LD. Similar analysis applied to all 13 HEAs are shown in Supplementary Table 1 and Supplementary Fig. 5. The largest (smallest) sum of FWHM is in M8 (M1), which coincides with the supercell volume (Table 1). However, there is little resemblance in the relative ranking of the volume and the sum of FWHM. FWHM is extracted from the distribution of BO values calculated quantum mechanically, whereas volume is a structural parameter that does not involve detailed interactions among the atoms. Thus, LD in HEAs can now be rigorously quantified that are difficult to capture in experiments. For example, neutron scattering may reveal the NN distance, but not the detail of the SNN distance. This trend contributes to the difficulties in discussing the LD from experimental data. In the 4-component HEA such as M1 (TiNbTaV) there are 10 distinctively different NN pairs. In the 5-component HEA M5 (NbTaTiVZr), there are 15 NN pairs. The ab initio modeling can facilitate the interpretation of the experimental data. For example, based on the neutron (synchrotron) diffraction measurements, Lee et al. estimated the NN distance in M1³⁶ and M5³⁷ to be 2.788 (2.085 Å) and 2.863 (2.866 Å), respectively. These results compare very favorably with the calculated values of 2.786 and 2.854 Å (Supplementary Table 1), respectively. Both results show that adding Zr to M5 from M1, the average NN distance increased by

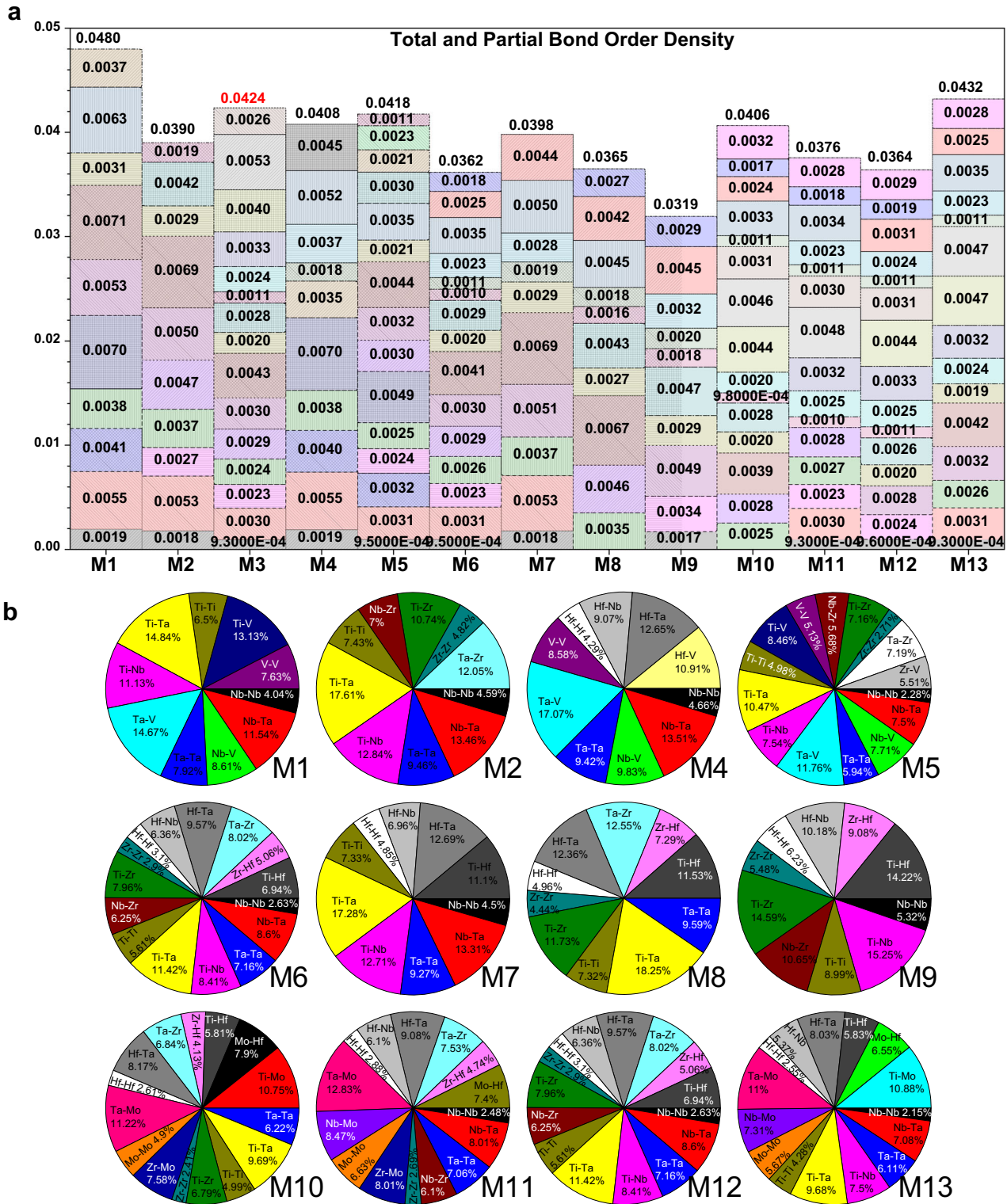


Fig. 2 Total and partial bond order density in units of electrons/ \AA^3 . **a** Histogram presentation of TBOD and PBOD for 13 models. Observations: (1) M1 has the highest TBOD of 0.0480 of $\text{e}^-/\text{\AA}^3$ and M9 has the lowest TBOD of 0.0319 of $\text{e}^-/\text{\AA}^3$. (2) The TBOD does not depend on the number of components (4 or 5). (3) There is no evidence that the size of the atom influences the PBOD. (4) There is some evidence that the Ti-Ta pair has a relatively large PBOD whereas the Nb-Nb pair has a relatively small PBOD. **b** Pie chart presentation for PBOD except M3 (in Fig. 1e).

only about 2.2% or 2.4% which is not a large LD envisioned. However, the calculated FWHM values for M1 and M5 (Supplementary Table 1) are 0.211 and 0.379 \AA respectively, an increase of

almost 80%. Obviously, the sum from NN and SNN FWHM is a more realistic estimation for the observed large LD due to the addition of Zr to M1 (TiNbTaV) observed experimentally.

Table 3. Mechanical properties comparison of calculated and experimental data in 13 HEAs.

Model	C_{11}	C_{12}	C_{44}	K		G		E		η		H_v	
				Calc.	Exp.	Calc.	Exp.	Calc.	Exp.	Calc.	Exp.	Calc.	Exp.
M1	217.33	132.09	29.09	160.43	146.6 ⁽²⁾³⁷ 139.0 ⁽¹⁾³⁷	33.79	42.9 ⁽²⁾³⁷ 44.2 ⁽¹⁾³⁷	94.73	108.00 ³⁸ 117.3 ⁽²⁾³⁷ 119.9 ⁽¹⁾³⁷	0.402	0.368 ⁽²⁾³⁷ 0.356 ⁽¹⁾³⁷	1.893	2.923 ³⁹
M2	167.56	111.81	34.61	130.39	—	31.72	—	88.02	115.00 ⁽⁵⁾⁴⁰	0.388	—	2.132	3.200 ⁴⁰
M3	207.45	119.69	33.20	148.89	—	37.05	—	102.65	153.00 ⁽⁶⁾⁴¹	0.385	—	2.442	4.900 ⁴¹
M4	203.29	126.71	35.27	152.23	—	36.40	—	101.14	—	0.389	—	2.304	—
M5	174.02	113.93	29.99	133.94	138.4 ⁽²⁾³⁷	29.98	36.6 ⁽²⁾³⁷	83.70	100.9 ⁽²⁾³⁷	0.396	0.379 ⁽²⁾³⁷	1.863	—
M6	154.08	108.90	37.38	123.84	134.60 ⁽³⁾⁴²	30.52	28.00 ⁽³⁾⁴²	84.61	85.00 ⁽⁴⁾⁴³	0.386	0.402 ⁽³⁾⁴²	2.105	2.893 ⁴⁴
M7	178.70	118.79	42.12	138.73	—	36.73	—	101.25	—	0.378	—	2.603	—
M8	141.22	101.91	39.71	114.63	—	29.92	—	82.57	—	0.380	—	2.215	—
M9	139.60	98.72	37.11	112.15	105.7 ⁽¹⁾⁴⁵	29.17	25.1 ⁽¹⁾⁴⁵	80.53	69.7 ⁽¹⁾⁴⁵	0.380	0.309 ⁽¹⁾⁴⁵	2.168	—
M10	180.92	109.24	41.55	133.12	—	39.14	—	106.94	—	0.366	—	3.068	5.315 ⁴⁶
M11	204.98	118.28	35.42	147.13	—	38.35	—	105.86	—	0.380	—	2.638	—
M12	177.43	105.78	32.91	129.63	—	33.99	—	93.78	—	0.379	—	2.438	—
M13	217.54	125.81	38.38	156.35	—	41.15	—	113.50	—	0.379	—	2.804	—

Elastic coefficient C_{ij} , bulk modulus (K), shear modulus (G), and Young's modulus (E) in unit of GPa in 13 HEAs. η is the Poisson's ratio and H_v is the estimated Vickers hardness. Experimental data with references using different techniques are indicated at bottom. The superscript: ⁽¹⁾resonant ultrasound spectroscopy; ⁽²⁾in-situ neutron; ⁽³⁾ultrasound spectroscopy; ⁽⁴⁾compression; ⁽⁵⁾nano-indentation; ⁽⁶⁾use Vickers hardness testing.

Mechanical properties

One of the most important properties of HEAs is the mechanical properties. They are intimately related to the electronic structure and bonding (see "Methods" section). The calculated results of the 13 HEAs include the elastic coefficients, compliance tensor, bulk modulus (K), shear modulus (G), Young's modulus (E), Poisson's ratio (η), G/K ratio and estimated Vickers hardness (H_v) together with the available experimental data^{37–46} is presented in Table 3. The experimental data for refractory BCC HEAs are quite limited. Of the 13 models listed, there are no experimental data for (M4, M7, M11, M12, and M13). M10 has data for H_v only, while M2 and M3 have results for E and H_v only. M5 and M9 lack H_v data. M1 is the only HEA having experimental data in every column to compare with the calculated values. The calculated H_v is based on a formula suggested by Tian et al.⁴⁷ from the fitted data to MGs and is generally underestimated from the measured data. The experimental data for HEAs have considerable variations due to the uncertainty in the composition and different methods used. Overall, the agreement with the limited experimental data is quite reasonable and consistent, especially for M6 and M9. The calculated Poisson's ratios for the 13 HEAs range from 0.366 (M10) to 0.402 (M1), which are on the ductile side. We plotted the G vs. K for all the 13 HEAs in Supplementary Fig. 6. The Pugh's ratio G/K is well within the range of 0.30 and 0.20 with the average around 0.25 which is on the ductile side for metallic systems, somewhere between bulk metallic glass (BMG) and polycrystalline metals⁴⁸. There is a good correlation between the calculated bulk modulus K and TBOD (Fig. 3), since the TBOD is a single metric that quantifies the internal cohesion. Correlations of TBOD with G and E are less obvious since they involve directional dependence in the strain.

Porosity in TiNbTaZrMo

For the biocompatible HEAs proposed for biomedical applications, the most relevant property is Young's modulus E , which range from 83.7 GPa for M5 (NbTaTiVZr) to 113.5 GPa for M13 (TiNbMoHfTa). To be compatible with the strengths of bones and joints in a human body, the E needs to be reduced by at least

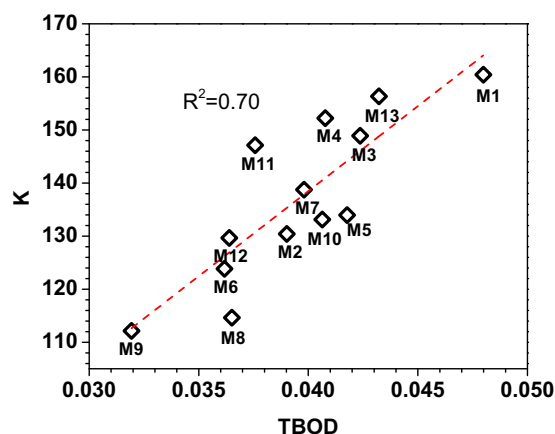


Fig. 3 Correlation of bulk modulus with TBOD in 13 HEAs. Dashed line is a linear fit that resulted from the coefficient of determination $R^2 = 0.70$ of bulk modulus (K) in GPa and TBOD in e/Å of the 13 investigated HEAs. This means the K is tightly correlated with TBOD.

50%. It is well known that there is a correlation between Young's modulus and the porosity in porous materials⁴⁹. We provide some preliminary test calculation by introducing porosity in the simulation for M3 to reduce E . Seven cases of porous models (p1–p6 and px) are constructed from the non-porous model or M3 (p0) by deleting a portion of connected atoms from p0 making sure that the atomic composition is still remain equal partition as in the original model. This is not an easy task but is necessary. The porosity values for each model from p0 to p6 and px are determined by using the PLATON software to be 0.0%, 2.90%, 4.00%, 7.50%, 11.2%, 18.2%, 23.5%, and 30.0%, respectively. These models are shown in Fig. 4a using Crystallite17 software.

The porosity can reduce Young's modulus significantly in M3 (Fig. 4b). Figure 4a shows that p6 with porosity of 23.5%, the E was reduced to 60.83 GPa from 102.65 GPa in p0, closer to E values exhibited by human cortical bones typically ranging from 7 to 30 GPa⁵⁰, but still way too large. The other porosity-dependent

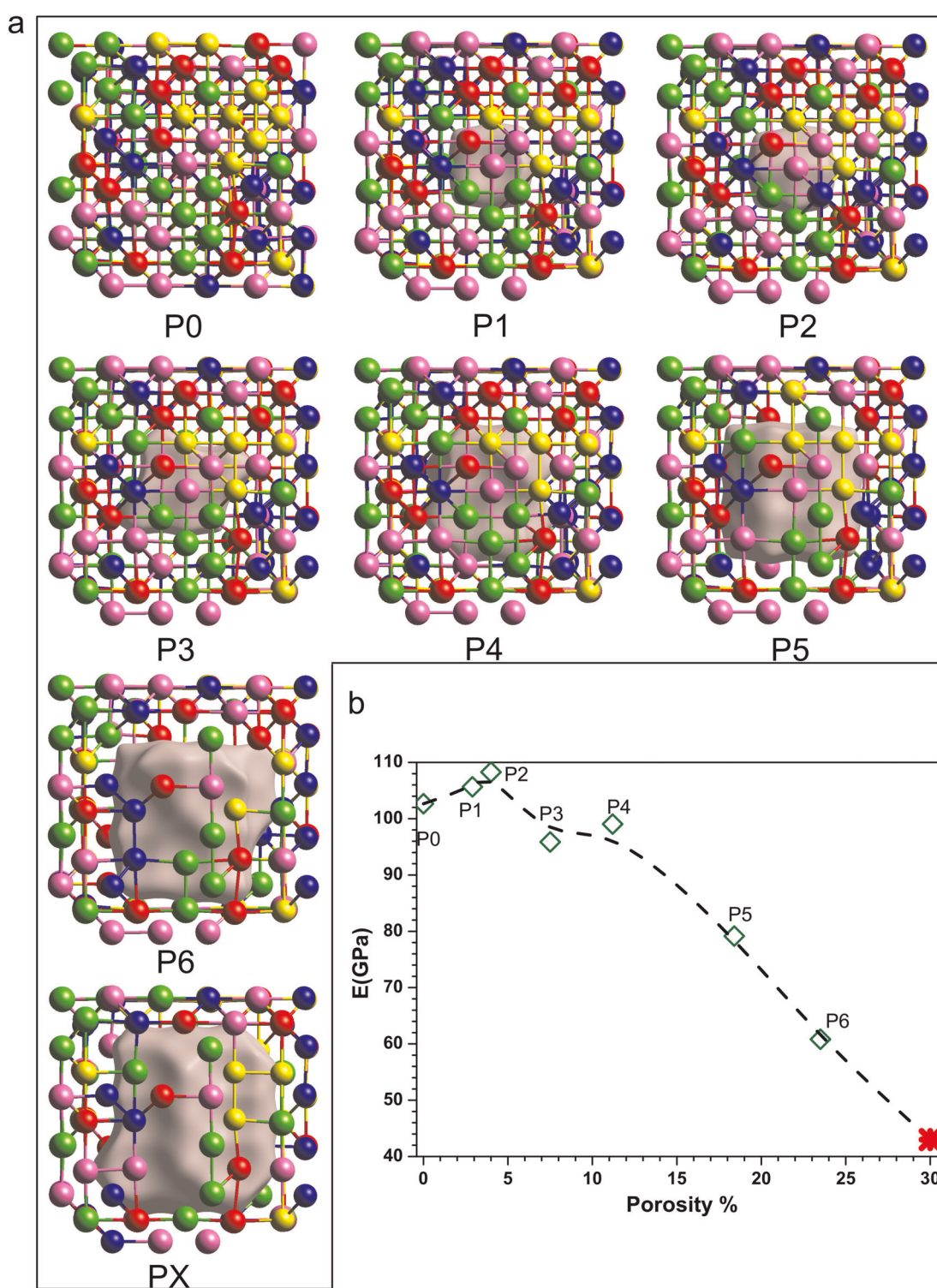


Fig. 4 Porosity modeling for M3. **a** Ball and stick models that exhibit different levels of porosity from p0 to px are plotted using the CrystalExplorer17 software. The different level of porosity is achieved by removing a portion of connected metal atoms in an equal proportion starting with p0 (no porosity) up to p6, which has a large single pore. These models are fully relaxed with the cell volume fixed and their mechanical properties are calculated in the same manner as for the 13 HEA models. **b** Young's modulus E vs. porosity. The data for porosity values from p1 to p3 contain some fluctuations due to the larger error/volume ratio of the small pores. When the modeling was applied to the model with largest porosity of 34.2% (px), the simulation failed to converge because the ratio of the size of the pore to p0 is too large.

mechanical properties also show similar decrease in bulk and shear modulus with the Poisson's ratio decreases from 0.39 at p0 to 0.30 at p6. This implies that the HEA represented by M3 becomes more brittle as the porosity is increased. However, this

point is less clear and requires detailed modeling for biocompatible HEAs in an aqueous environment. Another positive fact is that the introduction of porosity greatly reduce the weight of the materials, an important consideration for biomedical applications.

Currently, most biomedical applications involve the use of Ti alloys which is the lightest refractory element in the HEAs.

The current study on porosity simulation is limited to the starting supercell size of 250 atoms. A larger supercell containing 432 atoms (see Supplementary Materials) or even larger and with multiple smaller pores would be necessary for more realistic simulations. Young's modulus for the 432-atom supercell is 100.77 GPa, slightly <102.65 GPa for the 250-atom supercell (Supplementary Table 2). This exploratory study is to provide the proof-of-concept that supercell modeling can provide the guideline to reduce Young's modulus in biocompatible HEAs by introducing porosity of varying shapes that can accommodate bone structures in the human body. In doing so, our simulation method may facilitate the discovery of viable means to fabricate HEAs that are good candidates for biomedical applications.

DISCUSSION

In this study, several new results with lasting impacts are revealed. (1) The use of quantum mechanical metrics, TBOD and PBOD, for the HEA research. (2) Accurate ab initio modeling for 13 biocompatible HEAs together with their mechanical properties. (3) Realistic calculation of the atomic charges on every atom showing the inadequacy of using the VEC as a valid parameter in the theory of HEAs. (4) Precise quantification of the degree of LD based on our approach of ab initio simulation. (5) Proof of concept in addressing the porosity effect critical for using HEAs for biomedical applications.

The method and approach we used here can be readily extended to other multi-phase HEAs, or composites with lighter nonmetallic elements, and the presence of defects or other special refractory elements, such as tungsten (W)⁵¹ greatly expanding its applicability. There is now a new trend to expand HEAs to composite materials, which contain light elements, such as C, B, N, and O (especially C) to form HEA ceramics^{32,33}. Although the random solid solution model may still hold, the supercell construction for the composites will be much more challenging because of the involvement of non-metallic elements. Other possible extensions of HEAs include the deviation from equal-atomic compositions or even the mixed phases to optimize certain properties. Last but not the least, more realistic modeling for biocompatible HEAs in aqueous solution or body fluid is possible. With the ever-increasing computing power, such large-scale computational modeling in complex materials is very realistic in the near future.

METHODS

Supercell construction

The cubic supercells for biocompatible high entropy-alloys (HEAs) in the BCC lattice are constructed based on the random solid solution model (RSSM). The size of the supercell, or the number of atoms N it contains BCC supercell is determined by the simple formula $N = 2 \times (n)^3$. In the present work, n is 5 so the supercell has 250 atoms in the cubic cell of length equal to na , where a is the lattice constant of the single atom BCC crystal of a typical transition metal. We believe that a 250-atom supercell may be the minimal size to justify the use the RSSM with sufficient confidence. It should be pointed out that our supercell is different from those used in the SQS structure in the simulations by other researchers which is usually much smaller. To account for the different possible structural configurations, many such so-called "supercells" have to be used. In the present study, we assert that the statistical distribution of random distribution of metals is sufficient, since the supercell is sufficiently large and with periodical boundary conditions and can account for the random distribution of the NN, second NN and also the third NN and beyond for each atom in the model. These two approaches are similar in spirit but different in strategy. We believe the use of large supercells for many HEAs is more efficient, tractable, and conducive for detailed bond analysis and calculation of TBOD. Four or five atomic species of equal percentage are

chosen from the following seven refractory elements: Ti, V, Zr, Nb, Mo, Hf, and Ta, and are distributed randomly in the lattice sites of the supercell with periodic boundaries. For the 5-component HEAs, there are 50 atoms each. For the 4-component HEAs, two of them have 62 atoms, and the other two have 63 atoms each. The initial lattice constant for the supercell is obtained from the scaled average of the crystal lattice constant for each atom. To fully comply with the spirit of RSSM, a script is written such that the atomic occupation of each site is completely random with no restriction to their NN atoms and beyond. So for the 4 (5)-component HEA models, the supercell will have 10 (15) possible NN pairs.

Structural relaxation

The initial BCC supercells for HEAs are fully optimized using the Vienna Ab initio Simulation Package (VASP)^{52,53}. VASP is a plane-wave-based DFT method using the pseudopotential. It is very efficient for the structural optimization and elastic properties calculations. In the present work, the PAW-PBE potential for the exchange correlation potential within the generalized gradient approximation (GGA) was used⁵⁴. We adopt a relatively high energy cutoff of 500 eV. The electronic and ionic force convergences were set at 10^{-5} eV and 10^{-3} eV/Å, respectively, with a $2 \times 2 \times 2$ k -point mesh. Additional testing with selected sample for higher k -point showed no discernable difference. The final relaxed structures of the 13 biocompatible HEAs (Table 1) based on which all the properties are evaluated. The sketch of the supercell for M3 is shown in Fig. 1a.

Electronic structure and interatomic bonding

For electronic structure and bonding calculations, the in-house developed package, the orthogonalized linear combination of the atomic orbitals (OLCAO) method is used⁵⁵ with the VASP-relaxed structures as the input. The OLCAO method is another DFT-based method using atomic orbitals for the basis expansion, which are expressed as a linear combination of Gaussian type of orbitals (GTO). The use of GTO enables the efficient evaluation of three center integrals in the analytic form and thus makes the method highly efficient, especially for large complex systems as demonstrated in many recent publications. In the present calculations for HEAs, a more localized minimal basis (MB) set is used, which consists of the core orbitals and the open shell of valence orbitals. Using Ti as an example, the MB has core orbitals of (1s, 2s, 2p, 3s, and 3p) and valence orbitals of (4s, 4p, and 3d).

In addition to the usual electronic structures such as DOS and partial DOS (PDOS), the most important part of the calculation is the effective charges Q_a^* and the BO values, $\rho_{\alpha\beta}$, between each pair of atoms (α, β) based on the Mulliken population analysis scheme⁵⁶:

$$Q_a^* = \sum_i \sum_{m,occ} \sum_{j,\beta} C_{ia}^{*m} C_{j\beta}^m S_{ia,j\beta} \quad (1)$$

$$\rho_{\alpha\beta} = \sum_{m,occ} \sum_{j,\beta} C_{ia}^{*m} C_{j\beta}^m S_{ia,j\beta} \quad (2)$$

In Eqs. (1) and (2), $S_{ia,j\beta}$ are the overlap integrals between the i th orbital in the α th atom and j th orbital in the β th atom. $C_{j\beta}^m$ are the eigenvector coefficients of the m th band for the j th orbital in the β th atom. The PC, ΔQ , or the charge transfer for each atom, is the deviation from neutral atomic charge (Q^0) from the effective charge (Q^*) or $\Delta Q = Q^0 - Q^*$. The accurate determination of PC is extremely important in interpreting many of the material properties and their functionality, especially in HEAs. This function arises from the multi-component nature of the HEAs, which consists of transition metal elements with different d -electron occupations. The BO value, $\rho_{\alpha\beta}$, between a pair of atoms in Eq. (2) provides a quantitative measure of the contribution to the metallic bond from atoms α and β with a specific distance of separation. This BO value is affected by the presence of all the nearby atoms which contribute to the BO. The summation of all BO values normalized by the cell volume gives us the TBOD, which is a single metric to assess the internal cohesion in the crystal⁵⁷. The TBOD can be resolved into partial components or the partial BO density (PBOD) for the different types of atomic pairs, or different groups of atoms in the structural units in the crystal or the supercell.

Mechanical properties

For the elastic and mechanical properties of the HEAs, we used the stress (σ_j) vs. strain (ϵ_j) response analysis scheme^{58,59} on the fully relaxed structure from VASP. A small strain ϵ ($\pm 0.5\%$) is applied to the supercell to obtain the elastic coefficients C_{ij} and compliance tensor S_{ij} ($i, j = 1, 2, 3, 4, 5$,

6) by solving the following set of linear equations:

$$\sigma_i = \sum_{j=1}^6 C_{ij} \varepsilon_j \quad (3)$$

From the calculated C_{ij} and S_{ij} , other mechanical properties such as the bulk modulus (K), shear modulus (G), Young's modulus (E), and Poisson's ratio (η) are obtained using the Voight–Reuss–Hill (VRH) polycrystalline approximation^{60–62}. More detailed information on the methods used for mechanical properties are described in the Supplementary Materials S1.

DATA AVAILABILITY

All the data in this paper including those in the supplementary materials are freely available by contacting the corresponding author (chingw@umkc.edu).

CODE AVAILABILITY

There are several software and packages were used for this study; the analyses were done using Crystallite17, Platon, and Origin software. Besides the Vienna ab initio structural Simulation Package (VASP)⁵³, the orthogonalized linear combination of the atomic orbitals (OLCAO)⁵⁵ method was used.

Received: 16 January 2020; Accepted: 31 March 2020;

Published online: 06 May 2020

REFERENCES

- Miracle, D. B. & Senkov, O. N. A critical review of high entropy alloys and related concepts. *Acta Mater.* **122**, 448–511 (2017).
- Gao, M. C., Yeh, J.-W., Liaw, P. K. & Zhang, Y. *High-entropy Alloys: Fundamentals and Applications* (Springer, 2016).
- Lim, X. Mixed-up metals make for stronger, tougher, stretchier alloys. *Nat. News* **533**, 306 (2016).
- Ye, Y., Wang, Q., Lu, J., Liu, C. & Yang, Y. High-entropy alloy: challenges and prospects. *Mater. Today* **19**, 349–362 (2016).
- Zhang, Y. et al. Microstructures and properties of high-entropy alloys. *Prog. Mater. Sci.* **61**, 1–93 (2014).
- Li, Z., Pradeep, K. G., Deng, Y., Raabe, D. & Tasan, C. C. Metastable high-entropy dual-phase alloys overcome the strength–ductility trade-off. *Nature* **534**, 227 (2016).
- Santodonato, L. J., Liaw, P. K., Unocic, R. R., Bei, H. & Morris, J. R. Predictive multi-phase evolution in Al-containing high-entropy alloys. *Nat. Commun.* **9**, 4520 (2018).
- Li, Q. J., Sheng, H. & Ma, E. Strengthening in multi-principal element alloys with local-chemical-order roughened dislocation pathways. *Nat. Commun.* **10**, 11 (2019).
- Ding, J., Yu, Q., Asta, M. & Ritchie, R. O. Tunable stacking fault energies by tailoring local chemical order in CrCoNi medium-entropy alloys. *Proc. Natl Acad. Sci. USA* **115**, 8919–8924 (2018).
- Sun, X. et al. Phase selection rule for Al-doped CrMnFeCoNi high-entropy alloys from first-principles. *Acta Mater.* **140**, 366–374 (2017).
- Zhang, F. et al. An understanding of high entropy alloys from phase diagram calculations. *Calphad* **45**, 1–10 (2014).
- Senkov, O. N., Senkova, S. V., Woodward, C. & Miracle, D. B. Low-density, refractory multi-principal element alloys of the Cr–Nb–Ti–V–Zr system: microstructure and phase analysis. *Acta Mater.* **61**, 1545–1557 (2013).
- LaRosa, C. R., Shih, M., Varvenne, C. & Ghazisaeidi, M. Solid solution strengthening theories of high-entropy alloys. *Mater. Charact.* **151**, 310–317 (2019).
- Tian, F. A review of solid-solution models of high-entropy alloys based on ab initio calculations. *Front. Mater.* **4**, <https://doi.org/10.3389/fmats.2017.00036> (2017).
- Widom, M. Modeling the structure and thermodynamics of high-entropy alloys. *J. Mater. Res.* **33**, 2881–2898 (2018).
- Sanchez, J. M., Vicario, T., Albizuri, J., Guraya, T. & Garcia, J. C. Phase prediction, microstructure and high hardness of novel light-weight high entropy alloys. *J. Mater. Res. Technol.* **8**, 795–803 (2019).
- Zunger, A., Wei, S. H., Ferreira, L. G. & Bernard, J. E. Special quasirandom structures. *Phys. Rev. Lett.* **65**, 353–356 (1990).
- Yang, Y., Wang, W., Gan, G.-Y., Shi, X.-F. & Tang, B.-Y. Structural, mechanical and electronic properties of (TaNbHfTiZr)C high entropy carbide under pressure: ab initio investigation. *Physica B: Condens. Matter* **550**, 163–170 (2018).
- Curatolo, S. et al. The high-throughput highway to computational materials design. *Nat. Mater.* **12**, 191–201 (2013).
- Chen, H. L., Mao, H. H. & Chen, Q. Database development and Calphad calculations for high entropy alloys: challenges, strategies, and tips. *Mater. Chem. Phys.* **210**, 279–290 (2018).
- Tian, F., Varga, L. K., Shen, J. & Vitos, L. Calculating elastic constants in high-entropy alloys using the coherent potential approximation: current issues and errors. *Comput. Mater. Sci.* **111**, 350–358 (2016).
- Huang, S., Tian, F. & Vitos, L. Elasticity of high-entropy alloys from ab initio theory. *J. Mater. Res.* **33**, 2938–2953 (2018).
- Miller, M. & Liaw, P. K. Bulk metallic glasses: an overview. in T. Egami (ed), *Atomistic theory of metallic liquids and glasses*, Chapter 2 (Springer Science & Business Media, 2008).
- Pelletier, J.-M. & Qiao, J. in J. D. Musgraves, J. Hu, L. Calvez (eds), *Springer Handbook of Glass* 617–643 (Springer, 2019).
- Ching, W.-Y. in J. D. Musgraves, J. Hu, L. Calvez (eds), *Springer Handbook of Glass* 1097–1130 (Springer, 2019).
- Gibon, E. et al. The biological response to orthopaedic implants for joint replacement: Part I: metals. *J. Biomed. Mater. Res. Part B* **105**, 2162–2173 (2017).
- An, Y. H. & Draughn, R. A. *Mechanical Testing of Bone and the Bone–Implant Interface* (CRC Press, 1999).
- Todai, M. et al. Novel TiNbTaZrMo high-entropy alloys for metallic biomaterials. *Scr. Mater.* **129**, 65–68 (2017).
- Diao, H. Y., Feng, R., Dahmen, K. A. & Liaw, P. K. Fundamental deformation behavior in high-entropy alloys: an overview. *Curr. Opin. Solid State Mater. Sci.* **21**, 252–266 (2017).
- Yang, K., Oses, C. & Curatolo, S. Modeling off-stoichiometry materials with a high-throughput ab-initio approach. *Chem. Mater.* **28**, 6484–6492 (2016).
- Troparevsky, M. C., Morris, J. R., Kent, P. R., Lupini, A. R. & Stocks, G. M. Criteria for predicting the formation of single-phase high-entropy alloys. *Phys. Rev. X* **5**, 011041 (2015).
- Sarker, P. et al. High-entropy high-hardness metal carbides discovered by entropy descriptors. *Nat. Commun.* **9**, 4980 (2018).
- Harrington, T. J. et al. Phase stability and mechanical properties of novel high entropy transition metal carbides. *Acta Mater.* **166**, 271–280 (2019).
- Dragoe, N. & Bérardan, D. Order emerging from disorder. *Science* **366**, 573–574 (2019).
- Wei, S. et al. Natural-mixing guided design of refractory high-entropy alloys with as-cast tensile ductility. Preprint at 1911.10975 (2019).
- Lee, C. et al. Lattice distortion in a strong and ductile refractory high-entropy alloy. *Acta Mater.* **160**, 158–172 (2018).
- Lee, C. et al. Temperature dependence of elastic and plastic deformation behavior of a ductile refractory high-entropy alloy. *Sci. Adv.* (2019) (in press).
- Couzinie, J. P., Senkov, O. N., Miracle, D. B. & Dirras, G. Comprehensive data compilation on the mechanical properties of refractory high-entropy alloys. *Data Brief.* **21**, 1622–1641 (2018).
- Yao, H. W. et al. NbTaV-(Ti,W) refractory high-entropy alloys: experiments and modeling. *Mater. Sci. Eng.: A* **674**, 203–211 (2016).
- Wang, S. P. & Xu, J. (TiZrNbTa)-Mo high-entropy alloys: dependence of microstructure and mechanical properties on Mo concentration and modeling of solid solution strengthening. *Intermetallics* **95**, 59–72 (2018).
- Wang, S. P. & Xu, J. TiZrNbTaMo high-entropy alloy designed for orthopedic implants: as-cast microstructure and mechanical properties. *Mater. Sci. Eng. C* **73**, 80–89 (2017).
- Dirras, G. et al. Elastic and plastic properties of as-cast equimolar TiHfZrTaNb high-entropy alloy. *Mater. Sci. Eng. A* **654**, 30–38 (2016).
- Gorsse, S., Nguyen, M. H., Senkov, O. N. & Miracle, D. B. Database on the mechanical properties of high entropy alloys and complex concentrated alloys. *Data Brief.* **21**, 2664–2678 (2018).
- Lin, C. M., Juan, C. C., Chang, C. H., Tsai, C. W. & Yeh, J. W. Effect of Al addition on mechanical properties and microstructure of refractory AlxHfNbTaTiZr alloys. *J. Alloy. Compd.* **624**, 100–107 (2015).
- Ye, Y. X. et al. Evaluating elastic properties of a body-centered cubic NbHfZrTi high-entropy alloy—a direct comparison between experiments and ab initio calculations. *Intermetallics* **109**, 167–173 (2019).
- Juan, C. C. et al. Enhanced mechanical properties of HfMoTaTiZr and HfMoNb-TaTiZr refractory high-entropy alloys. *Intermetallics* **62**, 76–83 (2015).
- Tian, Y. J., Xu, B. & Zhao, Z. S. Microscopic theory of hardness and design of novel superhard crystals. *Int. J. Refract. Met. Hard Mater.* **33**, 93–106 (2012).
- Greaves, G. N., Greer, A., Lakes, R. S. & Rouxel, T. Poisson's ratio and modern materials. *Nat. Mater.* **10**, 823 (2011).
- Kováčik, J. Correlation between Young's modulus and porosity in porous materials. *J. Mater. Sci. Lett.* **18**, 1007–1010 (1999).
- Bowen, P. K. et al. Biodegradable metals for cardiovascular stents: from clinical concerns to recent Zn-alloys. *Adv. Healthc. Mater.* **5**, 1121–1140 (2016).
- El-Atwani, O. et al. Outstanding radiation resistance of tungsten-based high-entropy alloys. *Sci. Adv.* **5**, eaav2002 (2019).
- Kresse, G. & Furthmüller, J. *Vienna ab-initio simulation package (VASP): The guide* (VASP Group, Institut für Materialphysik, Universität Wien, Sensengasse 8, 2002).
- Kresse, G. & Furthmüller, J. Software vasp, vienna, 1999. *Phys. Rev. B* **54**, 169 (1996).

54. Perdew, J. P., Burke, K. & Ernzerhof, M. Generalized gradient approximation made simple. *Phys. Rev. Lett.* **77**, 3865 (1996).
55. Ching, W.-Y. & Rulis, P. *Electronic Structure Methods for Complex Materials: The Orthogonalized Linear Combination of Atomic Orbitals* (Oxford University Press, 2012).
56. Mulliken, R. S. Electronic population analysis on LCAO–MO molecular wave functions. I. *J. Chem. Phys.* **23**, 1833–1840 (1955).
57. Dharmawardhana, C., Misra, A. & Ching, W.-Y. Quantum mechanical metric for internal cohesion in cement crystals. *Sci. Rep.* **4**, 7332 (2014).
58. Nielsen, O. & Martin, R. M. First-principles calculation of stress. *Phys. Rev. Lett.* **50**, 697 (1983).
59. Yao, H., Ouyang, L. & Ching, W. Y. Ab initio calculation of elastic constants of ceramic crystals. *J. Am. Ceram. Soc.* **90**, 3194–3204 (2007).
60. Voigt, W. *Lehrbuch der Kristallphysik, Nachdruck, 1. Auflage, Teubner* (Berlin, Leipzig, B.G. Teubner, 1928).
61. Reuss, A. Account of the liquid limit of mixed crystals on the basis of the plasticity condition for single crystal. *Z. Angew. Math. Mech.* **9**, 49–58 (1929).
62. Hill, R. The elastic behaviour of a crystalline aggregate. *Proc. Phys. Soc. Sect. A* **65**, 349 (1952).

ACKNOWLEDGEMENTS

This research used the resources of the National Energy Research Scientific Computing Center supported by DOE under Contract No. DE-AC03-76SF00098 and the Research Computing Support Services (RCSS) of the University of Missouri System. We thank C. Lee, Prof. V. Keppens and B. L. Musico for the helpful discussion on experimental measurements of elastic properties using neutrons and ultrasonics. The project is partially supported by DOE-NETL grant DE-FE0031554 (R.S. and W.-Y.C.). S.S. was supported in part from funds provided by the University of Missouri-Kansas City, School of Graduate Studies. P.K.L. is supported by the National Science Foundation (DMR-1611180 and 1809640) and Department of Energy (FE0008855 and DE-FE-0011194) with Drs. J. Mullen, V. Cedro, R. Dunst, S. Markovich, G. Shiflet, and D. Farkas as program managers and the U.S. Army Office Project (W911NF-13-1-0438 and W911NF-19-2-0049) with the program managers, Drs. M.P. Bakas, S. N. Mathaudhu, and D.M. Stepp.

AUTHOR CONTRIBUTIONS

W.-Y.C., R.S., P.L. and M.Z. conceived the project. W.-Y.C. and S.S. performed the calculations, W.-Y.C. drafted the paper. S.S. made all figures. J.B. compiled the

references. All authors participated in the discussion and interpretation of the results. All authors edited and proofread the final manuscript.

COMPETING INTERESTS

The authors declare no competing interests.

ADDITIONAL INFORMATION

Supplementary information is available for this paper at <https://doi.org/10.1038/s41524-020-0321-x>.

Correspondence and requests for materials should be addressed to W.-Y.C.

Reprints and permission information is available at <http://www.nature.com/reprints>

Publisher's note Springer Nature remains neutral with regard to jurisdictional claims in published maps and institutional affiliations.



Open Access This article is licensed under a Creative Commons Attribution 4.0 International License, which permits use, sharing, adaptation, distribution and reproduction in any medium or format, as long as you give appropriate credit to the original author(s) and the source, provide a link to the Creative Commons license, and indicate if changes were made. The images or other third party material in this article are included in the article's Creative Commons license, unless indicated otherwise in a credit line to the material. If material is not included in the article's Creative Commons license and your intended use is not permitted by statutory regulation or exceeds the permitted use, you will need to obtain permission directly from the copyright holder. To view a copy of this license, visit <http://creativecommons.org/licenses/by/4.0/>.

© The Author(s) 2020